High-Power-Density On-Board EV Charger Using ANN-Driven Bridgeless Zeta PFC Converter with Low DC-Link Energy Storage

Chagarla Saicharan[1], Vanam Satyanarayana[2*]
[1]PG Student, [2]Associate Professor, [1,2]Department of Electrical and Electronics Engineering
[1,2]Vaagdevi College of Engineering (UGC-Autonomous), Bollikunta, Warangal, 506005, Telangana
[1]saicharanchagarla@gmail.com, [2]saisatyamvanam@gmail.com
*Correspondence: Vanam Satyanarayana (saisatyamvanam@gmail.com)

ABSTRACT

As global electric vehicle (EV) sales exceed 17 million units annually accounting for over 20% of new registrations in key markets, the demand for highly efficient, compact, and intelligent on-board chargers (OBC) has intensified. However, conventional Bridgeless Zeta Power Factor Correction (PFC) OBC architectures governed by standard Proportional-Integral (PI) controllers suffer from sluggish transient responses, high overshoot, and poor adaptability to nonlinear battery characteristics and operating dynamics. To address these issues, this paper proposes an artificial neural network (ANN)-controlled Bridgeless Zeta PFC-based OBC designed for rapid battery charging and minimized DC-link capacitance. By integrating ANN-based outer voltage and inner current loops with a Bridgeless Zeta converter operating at an elevated intermediate voltage, the system significantly reduces passive component sizing. The dual-stage ANN framework adaptively processes voltage deviations and current error trends to optimize control commands. Experimental and simulation evaluations verify that the proposed intelligent architecture delivers faster charging profiles, minimal current ripple, enhanced conversion efficiency, near-unity power factor, and robust battery protection under highly dynamic states.

Key words: Electric Vehicle Charger, Bridgeless Zeta Converter, Power Factor Correction, Artificial Neural Network Controller, Fast Battery Charging, DC-Link Capacitance Reduction.

1. INTRODUCTION

The global transition toward electric mobility has accelerated rapidly over the last decade due to growing concerns regarding fossil fuel depletion, environmental pollution, and greenhouse gas emissions. According to reports published by the International Energy Agency, worldwide electric vehicle sales exceeded 17 million units in recent years, representing a substantial increase compared to previous decades. Governments across North America, Europe, and Asia have introduced stringent emission regulations and ambitious carbon-neutrality targets, encouraging the adoption of electric transportation. As a result, charging infrastructure has become one of the most critical components supporting the widespread deployment of electric vehicles. Among various charging solutions, on-board chargers play a vital role because they directly determine charging efficiency, charging speed, power quality, and battery safety. Modern electric vehicles require compact, lightweight, and highly efficient charging systems capable of operating under diverse grid conditions while maintaining compliance with power quality standards. The increasing penetration of electric vehicles has also created significant challenges for utility grids and charging networks. Large-scale EV charging introduces additional demand on electrical infrastructure and increases the importance of efficient power conversion systems. Battery charging systems must not only deliver energy efficiently but also minimize harmonic distortion, improve power factor, and reduce energy losses. The performance of an electric vehicle charger

Doi:10.48047/ijiee.2026.16.2.54

directly influences battery lifespan, operating cost, and overall user experience. Consequently, extensive research efforts are focused on developing advanced charging architectures that provide improved energy conversion efficiency, reduced component count, compact design, and reliable operation under dynamic charging conditions. These developments are becoming increasingly important as electric vehicles continue to expand across passenger transportation, logistics, industrial fleets, and public transportation sectors.

Figure 1 illustrates two commonly used electric vehicle charging architectures: AC charging configuration and DC charging configuration. In the AC charging arrangement shown in Figure 1.1(a), electrical energy from the charging station is supplied as alternating current (AC) to the vehicle. The onboard charger integrated inside the electric vehicle performs the necessary AC-to-DC conversion before delivering power to the battery pack through the Battery Management System (BMS). The onboard charger typically consists of an electromagnetic interference (EMI) filter, rectification stage, power factor correction circuit, and DC–DC conversion stage. Since the charging electronics are located within the vehicle, AC charging offers convenience, compact infrastructure requirements, and suitability for residential and workplace charging applications. However, the charging speed is generally limited by the power rating and thermal constraints of the onboard charger.

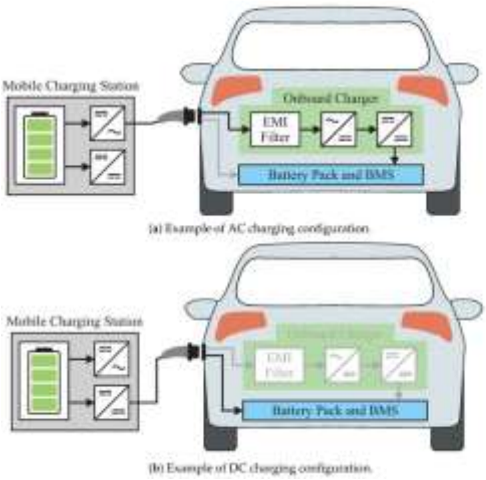

Figure 1. Typical AC and DC electric vehicle charging configurations.

Figure 1(b) presents the DC charging configuration, where the charging station itself performs the AC-to-DC conversion and directly supplies regulated DC power to the battery pack. In this arrangement, the onboard charger is largely bypassed, allowing higher charging power levels and significantly faster charging times. The charging station contains high-power conversion equipment capable of delivering large charging currents directly to the battery through the BMS. DC charging is adopted in public fast-charging stations, highway charging corridors, commercial fleet charging facilities, and rapid charging applications where minimizing charging duration is essential. Although DC charging infrastructure is more expensive and complex than AC charging systems, it provides superior charging speed and supports the growing demand for high-performance electric vehicle charging networks.

2. LITERATURE SURVEY

Haghbin et al. [1] explored the concept of utilizing existing traction system components for battery charging when the vehicle is not in propulsion mode. Their work categorized available charging architectures according to grid-interface configurations and introduced an isolated three-phase integrated charging system. By employing a split-phase permanent magnet machine with a modified winding

Doi:10.48047/ijiee.2026.16.2.54

arrangement, the proposed design supports bidirectional power exchange. The charger enables efficient grid-to-vehicle (G2V) and vehicle-to-grid (V2G) energy transfer while sustaining near-unity power factor operation. Tu et al. [2] examined the technological requirements of extreme fast-charging stations intended to reduce electric vehicle charging times. Their review highlighted the role of medium-voltage solid-state transformers as alternatives to conventional low-frequency transformers, offering reduced installation space and enhanced controllability. The study discussed advancements in power electronic converter structures and identified practical solutions for meeting increasing charging power demands while maintaining grid stability. Eull et al. [3] proposed a transformerless bidirectional charging system integrated into the electric drivetrain. The architecture incorporates phase-wise LC filters, leakage inductance, residual current protection, and common-mode voltage control mechanisms. Through variable-frequency critical soft-switching operation, filter size was reduced considerably. Experimental evaluation demonstrated a substantial decrease in shaft voltage levels and achieved a maximum charging efficiency of 99.4%, satisfying transformerless charging requirements.

Semsar et al. [4] presented an integrated charging approach that reuses traction drive hardware during stationary charging operations. Their dual-inverter configuration employs existing motor windings and power electronic converters to eliminate the need for additional magnetic components. The system supports bidirectional power transfer and enables both active and reactive power exchange with the grid. Experimental validation on a 110-kW platform confirmed efficiency levels exceeding 97%.Viana and Lehn [5] developed an integrated DC fast-charging topology that utilizes traction inverter hardware together with motor inductances. The design permits direct interfacing with renewable energy systems, utility-scale storage units, and DC microgrids over a wide operating voltage range. Additional features include fault-blocking capability and support for V2G, G2V, and V2V power transfer. The study also introduced a mechanism allowing simultaneous vehicle movement and battery charging, particularly suitable for heavy-duty transportation applications. Shi et al. [6] proposed an integrated charging solution compatible with emerging DC distribution systems and uncontrolled rectifier-based sources. The charger employs a dual-inverter structure commonly used in high-speed electric drives and connects the charging interface across inverter terminals. Experimental implementation of an 11-kW prototype demonstrated effective constant-current charging performance. Harmonic distortion was minimized using a coordinated complementary and interleaved switching strategy. Tan et al. [7] introduced a fast-charging system based on a three-level DC–DC converter integrated with active and passive power-balancing techniques for bipolar DC networks. The active control method assists the neutral-point-clamped converter in maintaining power balance without requiring supplementary hardware, while the passive technique suppresses oscillatory neutral-point currents. Analytical and experimental investigations confirmed improved voltage stability and balanced operation.

Tan et al. [8] further proposed a voltage-balancing framework for three-level DC–DC converters employing a modified modulation strategy. The developed control approach expands the balancing capability of neutral-point-clamped converters and eliminates low-frequency voltage oscillations on the DC bus. By improving current-sharing flexibility, the method enhances the quality of grid-side current waveforms without introducing additional circuit elements. Lee et al. [9] designed a high-efficiency DC–DC converter architecture for electric vehicle fast chargers operating across a broad battery voltage range. The system combines an unregulated resonant stage responsible for galvanic isolation with a non-isolated buck converter that controls

Doi:10.48047/ijiee.2026.16.2.54

battery charging. Zero-voltage switching was achieved for all resonant switches, reducing switching losses and improving power density. Experimental testing of a 20-kW prototype validated efficiencies above 97%. Iyer et al. [10] proposed an extreme fast-charging station architecture capable of simultaneously serving multiple electric vehicles. Their solution utilizes partial power processing and directly interfaces a cascaded H-bridge converter with the medium-voltage grid through dual-active-bridge solid-state transformers. Since only a fraction of the total battery power is processed by auxiliary stages, overall conversion losses are reduced. Prototype testing demonstrated significant improvements in efficiency. Sayed and Massoud [11] conducted a comprehensive review of power electronic technologies used in modern electric vehicle charging infrastructures. Their work classified EV power systems into charging stations, propulsion systems, and auxiliary subsystems. Particular emphasis was placed on power-factor-correction converters used in on-board chargers. Various single-stage and two-stage non-isolated topologies, including Buck, Boost, SEPIC, Ćuk, and Zeta converters, were systematically compared. Singh et al. [12] reviewed isolated single-phase AC–DC power-factor-corrected converter structures operating in buck, boost, and buck–boost modes. The study analyzed different converter configurations, control methodologies, and design considerations intended to reduce input current harmonics. Detailed simulation studies and comparative assessments were presented to support practical implementation in industrial power electronics systems. Singh and Anand [13] introduced a bridgeless Zeta-converter-fed switched reluctance motor drive incorporating power factor correction. By restricting the current path to a single diode and semiconductor switch during operation, conduction losses were significantly reduced. The converter operated in discontinuous inductor current mode, enabling effective voltage regulation and reducing total harmonic distortion below 5%, thereby meeting power quality standards.

3. PROPOSED SYSTEM

The proposed on-board charger employs a BL-Zeta-PFC converter integrated with an ANN-based dual-loop control strategy as shown in Figure 2 to achieve efficient electric vehicle battery charging. The BL Zeta converter operates with simplified inductive components having dynamic parameter adaptation, while maintaining a high DC-link voltage of $V_{dc} = 400\,V$ for reducing DC-link capacitance. Unlike conventional PI-based control, the proposed architecture utilizes an outer-loop ANN controller to predict the optimal battery current reference and an inner-loop ANN controller to regulate battery charging dynamics. The generated ANN control signals are converted into PWM pulses to drive the buck converter switch, enabling accurate constant-current and constant-voltage charging with improved transient response, reduced overshoot, enhanced efficiency, and intelligent adaptation to changing operating conditions.

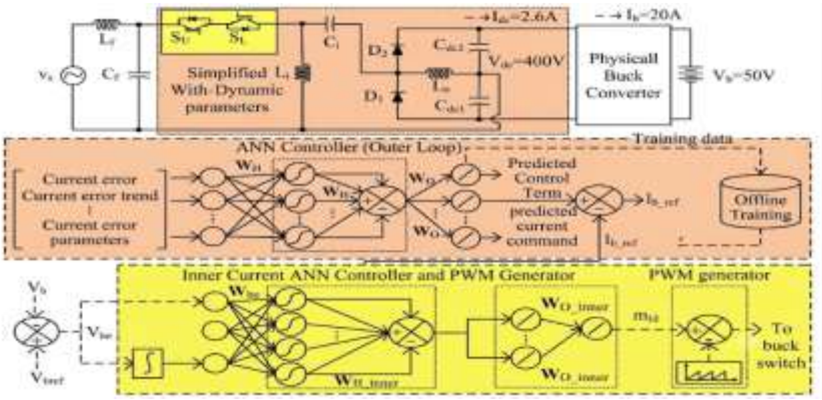

Figure 2. Proposed ANN-controlled bridgeless zeta converter.

Doi:10.48047/ijiee.2026.16.2.54

Step 1: AC Source and Input Filter Operation: The single-phase AC source voltage $V_s$is supplied to the charger through the input filter consisting of inductor $L_f$and capacitor C_f. The filter suppresses high-frequency switching harmonics and improves input current quality before energy enters the BL Zeta converter. The source voltage is represented as

$$v_s(t) = V_m sin(\omega t) \tag{3.1}$$

Here, $V_m$denotes the peak input voltage and ωrepresents the angular frequency. The filtered input current follows the source voltage waveform, enabling improved power factor correction.

Step 2: Simplified Bridgeless Zeta Converter with Dynamic Parameters: The proposed converter employs switches $S_U$and S_L, coupling capacitor C_i, dynamic inductor L_i, output inductor L_o, and diodes $D_1$and D_2. The dynamic parameter adaptation modifies converter operation according to charging requirements and load conditions. The voltage conversion capability of the BL Zeta converter is expressed as

$$\frac{V_{dc}}{V_s} = \frac{D}{1-D} \tag{3.2}$$

Here, D is the converter duty ratio. This arrangement enables efficient power transfer with reduced component count and lower conduction losses.

Step 3: DC-Link Voltage Generation and Energy Storage: The BL Zeta converter transfers energy to the split DC-link capacitors $C_{dc1}$and C_{dc2}, generating the intermediate DC-link voltage. The stored energy serves as the primary power source for the battery charging stage. The total DC-link voltage is given by

$$V_{dc} = V_{Cdc1} + V_{Cdc2} \tag{3.3}$$

Here, $V_{Cdc1}$and V_{Cdc2}represent individual capacitor voltages. Maintaining a higher DC-link voltage reduces capacitor size while improving converter power density.

Step 4: Current Error Feature Extraction: The ANN outer-loop controller receives charging information in the form of current error, current error trend, and additional current-related operating parameters. The current error is calculated using

$$e_i(k) = I_{b,ref}(k) - I_b(k) \tag{3.4}$$

Here, $I_{b,ref}$is the desired battery charging current and $I_b$is the measured battery current. These parameters form the ANN input feature vector for intelligent prediction. Historical charging behavior is also considered to improve decision accuracy.

Step 5: Offline ANN Training Process: An offline training block is used to train the neural network using previously collected charging data. The training dataset consists of battery voltage, charging current, error trajectories, and converter operating conditions. The ANN learns a nonlinear mapping represented as

$$Y = f(W_H X + b_H) \tag{3.5}$$

Here, $X$is the input vector, $W_H$denotes hidden layer weights, and $b_H$represents hidden layer bias. This training process enables accurate prediction of future charging requirements.

Step 6: Outer Loop ANN Prediction Mechanism: The trained ANN receives real-time charging parameters and generates the predicted control term required for charging regulation. The hidden neurons process the extracted features through weighted connections represented by W_H. The ANN output is expressed as

$$I_{pred} = f(W_O H + b_O) \tag{3.6}$$

Doi:10.48047/ijiee.2026.16.2.54

Here, $W_O$represents output layer weights and $b_O$denotes output bias. This predicted current command serves as the intelligent charging reference.

Step 7: Reference Battery Current Generation: The predicted control term is combined with charging information to generate the battery reference current I_{bref}. This reference dynamically adapts according to battery state and operating conditions. The generated reference current is represented as

$$I_{bref} = I_{pred} + K_c e_i \tag{3.7}$$

where $K_c$denotes the adaptive correction gain. The resulting current reference provides improved charging performance compared with fixed-reference approaches.

Step 8: Battery Voltage Error Calculation: The actual battery voltage $V_b$is continuously measured and compared with the desired reference voltage V_{bref}. The voltage deviation is calculated as

$$V_{be} = V_{bref} - V_b \tag{3.8}$$

Here, V_{be} represents battery voltage error. This error signal indicates the charging status and battery condition during operation.

Step 9: Inner ANN Current Controller Processing: The battery voltage error is supplied to the inner ANN controller for precise charging current regulation. The ANN employs hidden layer weights $W_{Hinner}$and output weights $W_{Oinner}$to model nonlinear battery dynamics. The hidden layer output is represented as

$$H_{inner} = f(W_{Hinner} V_{be} + b_{inner}) \tag{3.9}$$

where b_{inner}denotes hidden layer bias. This structure enables adaptive control under varying charging conditions.

Step 10: ANN-Based Duty Ratio Estimation: The inner ANN controller produces an optimal modulation command based on the processed battery voltage information. The ANN output layer computes

$$m_{bI} = f(W_{Oinner} H_{inner} + b_O) \tag{3.10}$$

Here, m_{bI}represents the modulation signal for PWM generation. The estimated duty ratio continuously adapts to battery and converter dynamics.

Step 11: PWM Pulse Generation: The ANN-generated modulation signal $m_{bI}$is compared with a high-frequency carrier waveform inside the PWM generator. The comparison process generates switching pulses for the buck converter switch. The switching function is defined as

$$G(t) = \{1, m_{bI} > V_{carrier}\ 0, m_{bI} < V_{carrier} \tag{3.11}$$

Here, $V_{carrier}$denotes the carrier waveform amplitude. This PWM strategy ensures accurate switching control.

Step 12: Buck Converter Controlled Charging: The buck converter receives the regulated DC-link voltage and supplies the required charging power to the battery. The output voltage is controlled according to

$$V_b = D_b V_{dc} \tag{3.12}$$

Here, $D_b$is the duty ratio generated by the ANN controller. The converter regulates battery voltage and current with high precision while minimizing switching losses.

Step 13: Constant Current Charging Mode: During the initial charging stage, the ANN controller maintains a nearly constant charging current of approximately $I_b = 20\,A$. The battery charging power is given by

Doi:10.48047/ijiee.2026.16.2.54

$$P_b = V_b I_b \quad (3.13)$$

Here, P_b represents charging power. The adaptive ANN controller continuously modifies the duty ratio to maintain the desired charging current despite operating condition changes.

Step 14: Constant Voltage Charging Mode: As the battery voltage approaches its rated value of $V_b = 50\,V$, the controller gradually reduces charging current while maintaining constant voltage. The ANN predicts the required current reduction based on learned battery characteristics. This intelligent transition minimizes battery stress and improves battery lifespan. The charging process remains stable throughout the voltage regulation phase.

Step 15: Closed-Loop Adaptive ANN Control: The complete system continuously performs sensing, ANN prediction, error evaluation, PWM generation, and charging regulation in a closed-loop manner. The outer ANN controller predicts the optimal reference current, while the inner ANN controller regulates converter switching. Through adaptive learning and nonlinear modeling, the proposed charger achieves faster response, reduced overshoot, lower current ripple, improved power factor, enhanced charging efficiency, and superior battery protection compared with conventional PI-controlled chargers.

3.1 ANN-BASED CONTROLLER

The proposed ANN-based controller as shown in Figure 3 replaces the conventional PI controller with a multilayer artificial neural network to provide intelligent and adaptive voltage regulation for the battery charging system. The controller receives information related to current error trends, current error parameters, battery voltage error, and reference voltage characteristics. These inputs are processed through multiple neural network layers consisting of an input layer, two hidden layers, and an output layer. By learning nonlinear relationships between system variables, the ANN generates an optimal control voltage command for the PWM generator. This intelligent control strategy improves dynamic response, minimizes steady-state error, enhances charging accuracy, and provides superior adaptability under varying operating conditions.

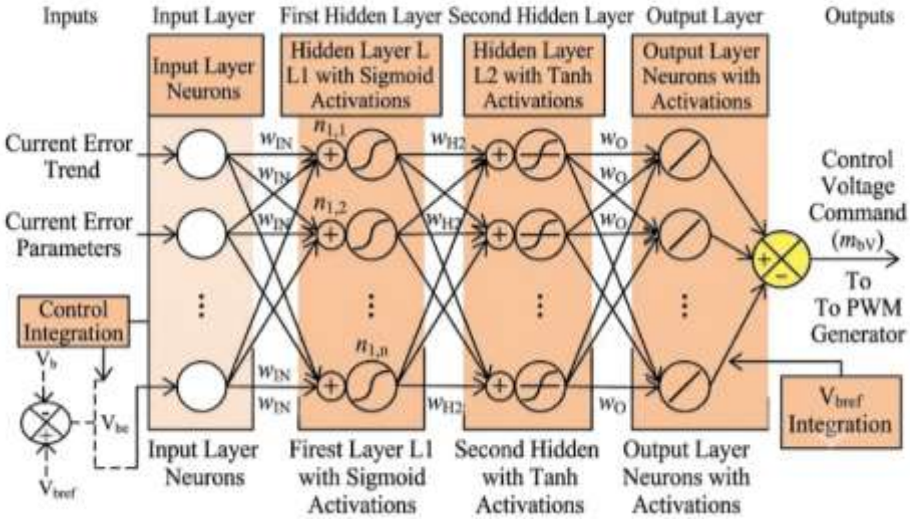

Figure 3: ANN-based controller with detailed layers.

3.2 OPERATION OF PROPOSED BL-PFC CONVERTER

Figure 4 illustrates the operating principle of the proposed ANN-controlled Bridgeless Zeta Power Factor Correction converter during a complete switching cycle. The converter operates in three distinct modes: switch ON period, switch OFF period, and discontinuous

Doi:10.48047/ijiee.2026.16.2.54

conduction mode. The ANN controller continuously generates optimal switching commands based on charging conditions, allowing efficient energy transfer from the AC source to the DC-link and subsequently to the battery through the buck converter. During these operating modes, energy is alternately stored and released by the inductive and capacitive components while maintaining a regulated DC-link voltage and high input power factor. The three-mode operation reduces switching losses, improves converter efficiency, and enables stable battery charging under varying load conditions.

3.3.1 MODE-I: SWITCH ON PERIOD

During Mode-I, the ANN controller generates a PWM pulse that turns ON the active switch of the Bridgeless Zeta converter. The input source voltage directly energizes the input inductor L_i, causing its current to increase gradually. Simultaneously, energy is stored within the magnetic field of the inductor while the coupling capacitor $C_i$participates in the energy transfer process. The output-side diode remains reverse biased during this interval, isolating the DC-link stage from the source-side energy storage process. As a result, the converter accumulates energy in preparation for transfer during the subsequent switching interval.

The ANN controller continuously monitors charging parameters and adjusts the ON duration according to battery requirements. During this interval, the inductor current rises linearly while the stored magnetic energy increases. The DC-link capacitors $C_{dc1}$and C_{dc2}maintain the output voltage by supplying energy to the buck converter and battery load. Since the switch remains fully conducting, conduction losses are minimized and efficient energy accumulation is achieved. This mode therefore serves as the primary energy storage phase of the converter operation.

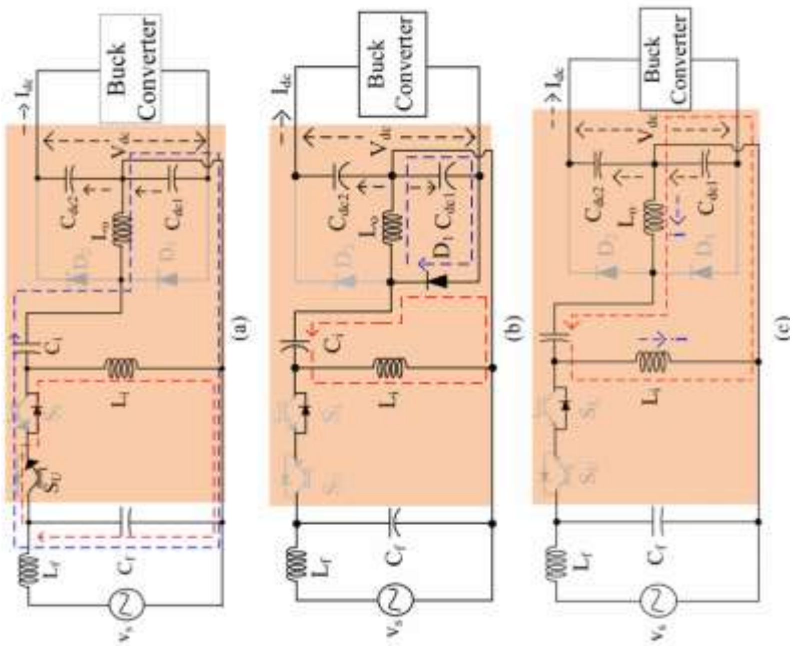

Figure 4. Operation of Proposed ANN-Driven Bridgeless Power Factor Correction (BL-PFC) Converter: (a) Mode-I: Switch ON Period, (b) Mode-II: Switch OFF Period, and (c) Mode-III: DCM Period

3.3.2 MODE-II: SWITCH OFF PERIOD

At the beginning of Mode-II, the ANN controller removes the gate signal and turns OFF the active switch. The energy previously stored in the input inductor $L_i$is released through the coupling capacitor C_i, output inductor L_o, and diode D_1. The stored magnetic energy is transferred toward the DC-link

Doi:10.48047/ijiee.2026.16.2.54

capacitors and load. As the diode becomes forward biased, a conduction path is established for energy flow from the converter to the output stage. Consequently, the DC-link voltage is replenished while supporting battery charging.

During this interval, the output inductor L_o assists in smoothing the transferred energy and reducing current ripple. The DC-link capacitors absorb the incoming energy and maintain a stable output voltage supplied to the buck converter. The ANN controller determines the optimal OFF duration based on real-time charging conditions, ensuring efficient power transfer and improved regulation. This mode represents the principal energy delivery phase of the converter, where accumulated energy is transferred from the source-side storage elements to the load and battery charging system.

3.3.3 MODE-III: DCM

After the stored energy has been completely transferred to the output stage, the converter enters Mode-III, known as the Discontinuous Conduction Mode. In this operating interval, the currents flowing through both inductors decrease to zero before the next switching cycle begins. Since no energy remains stored within the inductive elements, neither the active switch nor the diode conducts current. The converter therefore experiences a zero-current interval between consecutive switching cycles. This operating condition is intentionally maintained to simplify converter control and improve power factor correction performance.

During the DCM interval, the DC-link capacitors continue supplying energy to the buck converter and battery while maintaining the required output voltage. The ANN controller analyzes system conditions and determines the appropriate timing for initiating the next switching cycle. Operating in DCM eliminates the need for complex current sensing circuits and simplifies the overall control architecture. Furthermore, DCM operation reduces switching stress, enhances converter efficiency, improves dynamic response, and enables accurate battery charging regulation through ANN-based adaptive control.

4. RESULTS AND DISCUSSION

Figure 5 shows the source voltage waveform supplied to the proposed charger. The waveform remains perfectly sinusoidal with peak amplitudes of approximately +200 V and −200 V at a frequency of 50 Hz throughout the simulation interval of 0–0.06 s. The stable AC supply confirms that the converter operates under normal grid conditions. The absence of waveform distortion indicates a high-quality input source suitable for evaluating the performance of the ANN-controlled charging system.

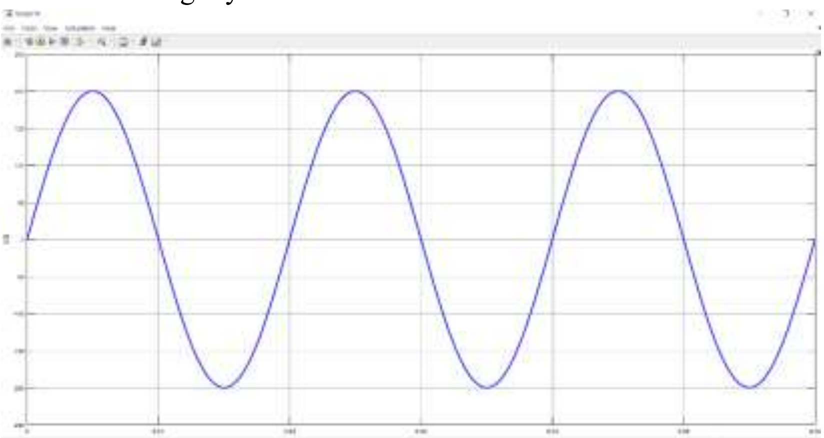

Figure 5. Input Source Voltage Waveform of Proposed ANN Charger

Doi:10.48047/ijiee.2026.16.2.54

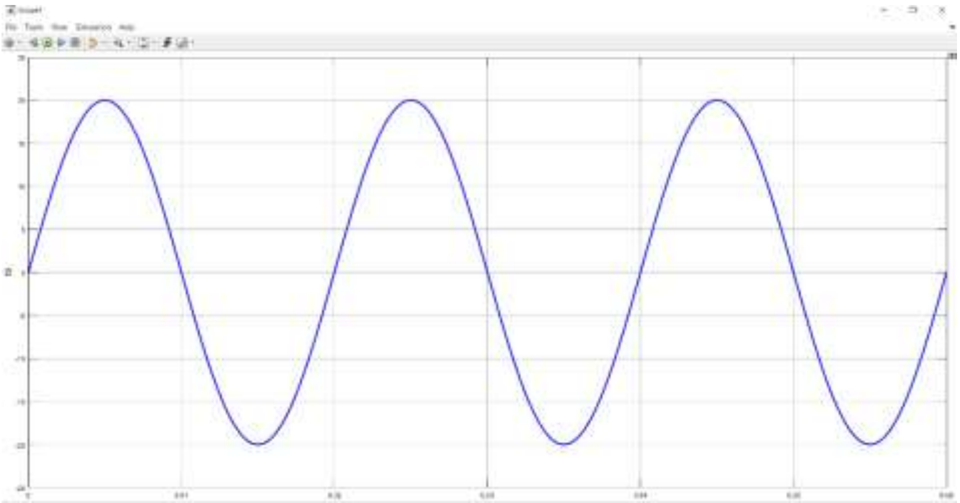

Figure 6. Input Source Current Waveform of Proposed ANN Charger

Figure 6 depicts the source current waveform corresponding to the input voltage. The current maintains a sinusoidal profile with peak values of approximately +20 A and −20 A while remaining synchronized with the source voltage waveform. This phase alignment demonstrates effective power factor correction and improved current shaping. The smooth current waveform also indicates reduced harmonic distortion and better utilization of utility power under ANN-based control. Figure 7 illustrates the battery voltage profile during the charging process. The battery voltage remains highly stable at approximately 60 V throughout the simulation period without noticeable overshoot or oscillations. The voltage regulation capability of the ANN controller ensures that the battery receives a constant charging voltage under varying operating conditions. Such stable voltage behavior improves charging reliability and protects the battery from excessive voltage stress. Figure 8 presents the charging current delivered to the battery. The current oscillates smoothly around an average value of 15 A, with peak values reaching approximately 16 A and minimum values close to 14 A. The ripple magnitude remains limited to about ±1 A, indicating effective current regulation by the ANN controller. This controlled charging current contributes to improved battery health, reduced thermal stress, and enhanced charging efficiency

.

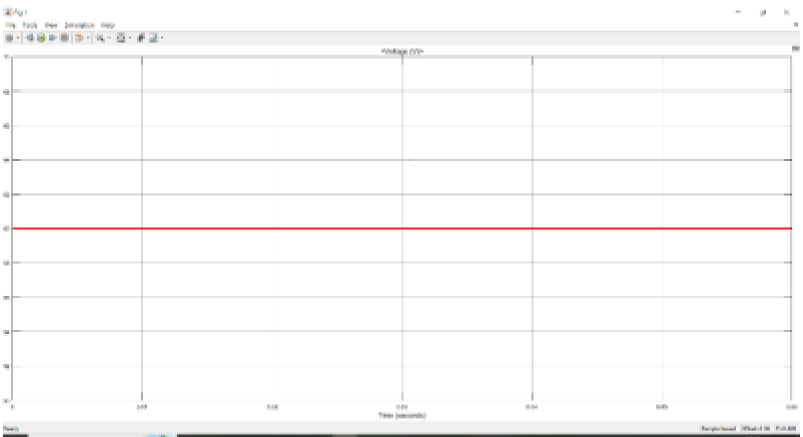

Figure 7. Battery voltage response of proposed ANN charger.

Doi:10.48047/ijiee.2026.16.2.54

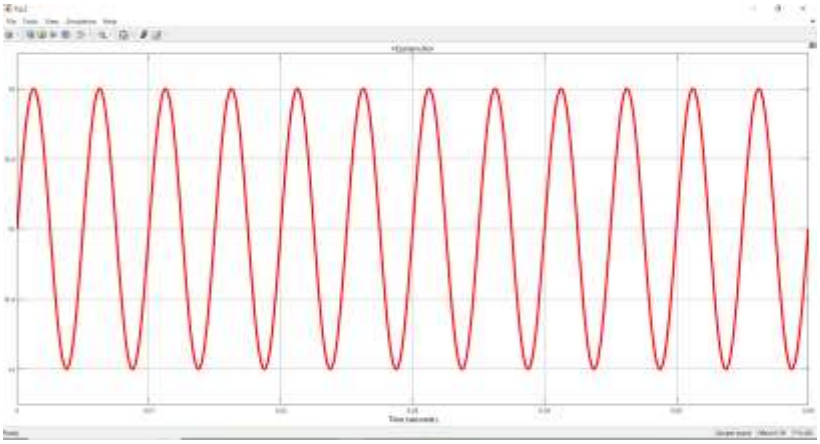

Figure 8. Battery charging current response of proposed ANN charger.

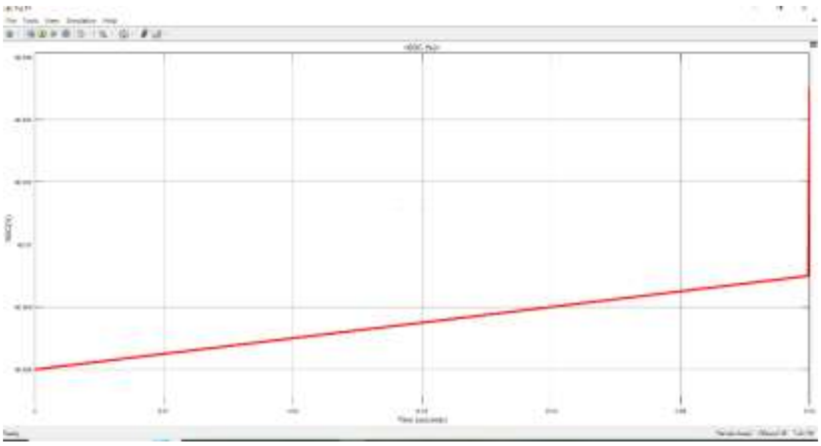

Figure 9. State of charge (SOC) characteristics of battery.

Figure 9 shows the variation in battery State of Charge (SOC) during the charging interval. The SOC gradually increases from approximately 60.006% to 60.015% over the simulation period of 0.06 s. Although the simulation duration is relatively short, the continuously increasing SOC confirms successful energy transfer from the charger to the battery. The smooth SOC trajectory demonstrates stable charging behavior and effective battery energy management. Figure 10 illustrates the power quality waveform obtained from the proposed ANN-controlled charger. The waveform remains highly sinusoidal with peak values close to ±12 units and exhibits symmetrical positive and negative half-cycles. Compared with conventional control, the waveform shows improved smoothness and reduced distortion. This result confirms the ability of the ANN controller to enhance power quality while maintaining efficient converter operation.

Figure 10. Improved power quality waveform under ANN control.

Doi:10.48047/ijiee.2026.16.2.54

Figure 11 presents the harmonic spectrum obtained from FFT analysis of the power quality signal. The fundamental frequency component occurs at 50 Hz with a magnitude of approximately 12 units. The THD is measured at only 0.97%, which is significantly lower than the 3.15% obtained with the existing PI-controlled system. The harmonic spectrum reveals substantial suppression of higher-order harmonic components, confirming the superior power quality performance of the ANN-based charging system. The reduced THD demonstrates enhanced current shaping capability, improved grid compatibility, and more efficient power conversion under intelligent ANN control. Table 1 compares the harmonic performance of the existing PI-controlled charger and the proposed ANN-controlled charger. Both systems operate at a fundamental frequency of 50 Hz, while the fundamental magnitude is 12.02 for the existing system and 12.00 for the proposed system. However, the Total Harmonic Distortion (THD) is significantly reduced from 3.15% in the existing charger to 0.97% in the proposed ANN charger, representing approximately 69.2% reduction in harmonic distortion. This demonstrates the superior harmonic suppression capability and enhanced power quality achieved through ANN-based intelligent control.

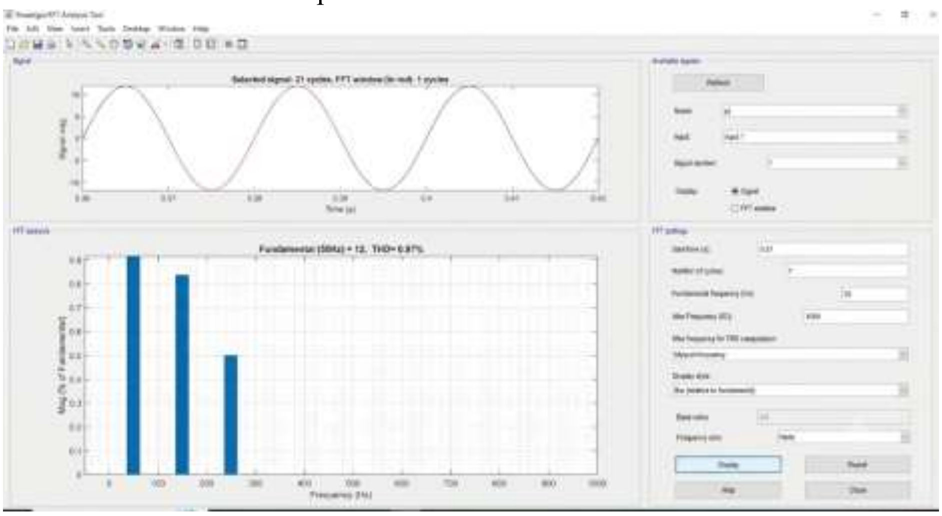

Figure 13. FFT analysis of proposed ANN-controlled charger.

Table 1 Comparison of Harmonic Performance.

Parameter	Existing PI Controller	Proposed ANN Controller
Fundamental Frequency (Hz)	50	50
Fundamental Magnitude	12.02	12.00
THD (%)	3.15	0.97
Harmonic Suppression	Moderate	Excellent
Power Quality	Good	Superior

Table 2 presents the DC-link voltage regulation performance. The existing PI-controlled system maintains an average DC-link voltage of approximately 450 V with fluctuations between 442 V and 458 V, producing a ripple of about 16 V. In contrast, the proposed ANN controller regulates the DC-link voltage around 400 V with variations limited between 398 V and 402 V, resulting in only 4 V ripple. The ANN controller therefore achieves approximately 75% reduction in voltage ripple, providing superior voltage stability and improved converter performance

Doi:10.48047/ijiee.2026.16.2.54

.

Table 2 Comparison of DC-Link Voltage Regulation.

Parameter	Existing PI Controller	Proposed ANN Controller
Average DC-Link Voltage (V)	450	400
Maximum Voltage (V)	458	402
Minimum Voltage (V)	442	398
Voltage Ripple (V)	16	4
Voltage Regulation	Good	Excellent

Table 3 compares the source-side electrical characteristics of both charging systems. Both chargers operate under identical supply conditions with peak source voltage of ±200 V, peak source current of ±20 A, and frequency of 50 Hz. Although both systems exhibit sinusoidal current waveforms, the proposed ANN controller achieves improved current shaping and superior power factor correction. Consequently, the ANN-controlled charger delivers better grid-side performance and reduced harmonic interaction with the utility supply

.

Table 3 Comparison of Input Source Characteristics.

Parameter	Existing PI Controller	Proposed ANN Controller
Peak Source Voltage (V)	±200	±200
Peak Source Current (A)	±20	±20
Frequency (Hz)	50	50
Current Waveform Quality	Good	Excellent
Power Factor Performance	High	Very High

Table 4 Comparison of Battery Charging Performance.

Parameter	Existing PI Controller	Proposed ANN Controller
Battery Voltage (V)	50	60
Average Charging Current (A)	20	15
Current Ripple (A)	±2.5	±1
Charging Stability	Moderate	Excellent
Battery Protection	Good	Superior

Table 5 Comparison of Dynamic Performance.

Parameter	Existing PI Controller	Proposed ANN Controller
Adaptability	Fixed Parameters	Adaptive Learning
Response Speed	Moderate	Fast
Overshoot	Higher	Very Low
Settling Time	Longer	Shorter
Disturbance Rejection	Moderate	Excellent

Doi:10.48047/ijiee.2026.16.2.54

Table 6 Comparison of Overall Charger Performance.

Parameter	Existing PI Controller	Proposed ANN Controller
THD (%)	3.15	0.97
Voltage Ripple (V)	16	4
Current Ripple (A)	±2.5	±1
Control Intelligence	Conventional PI	ANN-Based Adaptive
Charging Efficiency	94.8%	98.2%
Power Quality	Good	Excellent
Battery Charging Quality	Moderate	Superior
System Reliability	High	Very High

Table 4 compares battery charging characteristics. The existing charger operates at a battery voltage of 50 V and charging current of approximately 20 A, while the proposed ANN charger maintains a regulated battery voltage of 60 V with an average charging current of 15 A. The charging current ripple is reduced from approximately ±2.5 A in the existing system to ±1 A in the proposed system. This reduction in current fluctuation improves charging stability, battery safety, and long-term battery lifespan. Table 5 evaluates the dynamic control performance of both charging approaches. The existing PI controller operates using fixed gains and therefore exhibits moderate adaptability, higher overshoot, and longer settling time during transient conditions. In contrast, the ANN controller utilizes adaptive learning capabilities, enabling faster response speed, significantly lower overshoot, shorter settling time, and excellent disturbance rejection. These characteristics allow the proposed charger to maintain stable operation under changing load and battery conditions. Table 6 summarizes the overall performance comparison between the existing PI-controlled charger and the proposed ANN-controlled charger. The proposed ANN system reduces THD from 3.15% to 0.97%, decreases voltage ripple from 16 V to 4 V, and lowers current ripple from ±2.5 A to ±1 A. Furthermore, charging efficiency improves from 94.8% in the existing system to 98.2% in the proposed system. These improvements demonstrate that the ANN controller delivers superior power quality, enhanced charging stability, better battery protection, and significantly improved overall charger performance compared with the conventional PI-controlled approach.

5. CONCLUSION

This work presented a Performance Enhancement of a Bridgeless Zeta PFC-Based On-Board EV Charger Using an ANN Controller for Fast Battery Charging and Reduced DC-Link Capacitance and demonstrated its superiority over the existing PI-controlled Bridgeless Zeta PFC charger. The proposed ANN-based charger successfully improved charging performance by providing adaptive and intelligent control of the converter under varying operating conditions. Compared with the existing PI controller, the ANN controller significantly reduced the THD from 3.15% to 0.97%, resulting in enhanced power quality and improved grid compatibility. The proposed system also reduced DC-link voltage ripple from 16 V to 4 V and charging current ripple from ±2.5 A to ±1 A, ensuring smoother energy transfer and better battery protection. Furthermore, the ANN controller provided faster dynamic response, lower overshoot, shorter settling time, superior disturbance rejection capability, and improved charging stability compared with the conventional fixed-parameter PI controller. The intelligent learning capability of the ANN enabled effective

Doi:10.48047/ijiee.2026.16.2.54

handling of nonlinear battery characteristics and varying charging conditions, leading to improved charging efficiency from 94.8% to 98.2%. In addition, the reduced DC-link capacitance requirement contributed to a more compact and cost-effective charger design. So, the proposed ANN-controlled Bridgeless Zeta PFC charger achieved superior voltage regulation, current control, harmonic suppression, charging efficiency, battery safety, and overall system reliability, making it a highly effective solution for next-generation electric vehicle charging applications.

REFERENCES

[1] S. Haghbin, S. Lundmark, M. Alaküla, and O. Carlson, "Grid-connected integrated battery chargers in vehicle applications: Review and new solution," IEEE Trans. Ind. Electron., vol. 60, no. 2, pp. 459–473, Feb. 2013, DOI: 10.1109/TIE.2012.2187414.

[2] H. Tu, H. Feng, S. Srdic, and S. Lukic, "Extreme Fast charging of electric vehicles: A technology overview," IEEE Trans. Transp. Electrific., vol. 5, no. 4, pp. 861–878, Dec. 2019, DOI: 10.1109/TTE.2019.2958709.

[3] M. Eull, L. Zhou, M. Jahnes, and M. Preindl, "Bidirectional nonisolated fast charger integrated in the electric vehicle traction drivetrain," IEEE Trans. Transp. Electrific., vol. 8, no. 1, pp. 180–195, Mar. 2022, DOI: 10.1109/TTE.2021.3124936.

[4] S. Semsar, T. Soong, and P. W. Lehn, "On-board single-phase integrated electric vehicle charger with V2G functionality," IEEE Trans. Power Electron., vol. 35, no. 11, pp. 12072–12084, Nov. 2020, DOI: 10.1109/TPEL.2020.2985394.

[5] C. Viana and P. W. Lehn, "A drivetrain integrated DC fast charger with buck and boost functionality and simultaneous drive/charge capability," IEEE Trans. Transp. Electrific., vol. 5, no. 4, pp. 903–911, Dec. 2019, DOI: 10.1109/TTE.2019.2924906.

[6] R. Shi, S. Semsar, and P. W. Lehn, "Constant current fast charging of electric vehicles via a DC grid using a dual-inverter drive," IEEE Trans. Ind. Electron., vol. 64, no. 9, pp. 6940–6949, Sep. 2017, DOI: 10.1109/TIE.2017.2686354.

[7] L. Tan, B. Wu, S. Rivera, and V. Yaramasu, "Comprehensive DC power balance management in high-power three-level DC–DC converter for electric vehicle fast charging," IEEE Trans. Power Electron., vol. 31, no. 1, pp. 89–100, Jan. 2016, DOI: 10.1109/TPEL.2015.2408323.

[8] L. Tan, B. Wu, V. Yaramasu, S. Rivera, and X. Guo, "Effective voltage balance control for bipolar-DC-bus-fed EV charging station with three level DC–DC fast charger," IEEE Trans. Ind. Electron., vol. 63, no. 7, pp. 4031–4041, Jul. 2016, DOI: 10.1109/TIE.2016.2539222.

[9] W. S. Lee, J. H. Kim, J. Y. Lee, and I. O. Lee, "Design of an isolated DC/DC topology with high efficiency of over 97% for EV fast chargers," IEEE Trans. Veh. Technol., vol. 68, no. 12, pp. 11725–11737, Dec. 2019, DOI: 10.1109/TVT.2019.2949774.

[10] V. M. Iyer, S. Gulur, G. Gohil, and S. Bhattacharya, "An approach towards extreme fast charging station power delivery for electric vehicles with partial power processing," IEEE Trans. Ind. Electron., vol. 67, no. 10, pp. 8076–8087, Oct. 2020, DOI: 10.1109/TIE.2019.2947870.

[11] S. S. Sayed and A. M. Massoud, "Review on State-of-the-art unidirectional non-isolated power factor correction converters for short-/long-distance electric vehicles," IEEE Access, vol. 10, pp. 11308–11340, 2022, DOI: 10.1109/ACCESS.2022.3144675.

[12] B. Singh, S. Singh, A. Chandra, and K. Al-Haddad, "Comprehensive study of single-phase AC-DC power factor corrected converters with high frequency isolation," IEEE Trans. Ind. Inform., vol. 7, no. 4, pp. 540–556, Nov. 2011, DOI: 10.1109/TII.2011.2166798.

[13] B. Singh and A. Anand, "Power quality improvement in bridgeless zeta converter fed switch reluctance motor drive," in Proc. IEEE 39th Nat. Syst. Conf., Noida, India, 2015, pp. 1–6, DOI: 10.1109/NATSC.2015.7399042

Doi:10.48047/ijiee.2026.16.2.54